ITERATIVE WAVEFRONT RECONSTRUCTION IN ADAPTIVE OPTICS

QING CHU *

Abstract. Obtaining high resolution images of space objects from ground based telescopes is challenging, and often requires computational post processing using image deconvolution methods. Good reconstructions can be obtained if the convolution kernel can be accurately estimated. The convolution kernel is defined by the wavefront of light, and how it is distorted as it propagates through the atmosphere. In this paper we describe the wavefront reconstruction problem, and more specifically, a new linear least squares model that exploits information from multiple measurements.

Key words. image deblurring, multiframe deconvolution, least squares, astronomical imaging, wavefront reconstruction

AMS Subject Classifications: 65F20, 65F30

1. Introduction. When looking up to the sky, we can see stars sparkling. This phenomenon results when light passes through the turbulent atmosphere. The turbulence is caused by temperature fluctuations in the atmosphere, and consequently introduces refraction [10]. As a result, observation of spatial objects by ground-based telescopes will be degraded along the optical path through the atmosphere. Mathematically, this is modeled using a convolution formulation

$$g(x,y) = \int_{\mathcal{R}^2} k(x,y;\xi,\eta) f(\xi,\eta) d\xi d\eta + e_g(x,y) \tag{1.1}$$

where f is the true object, g is the observed image, and e_g is additive noise. The kernel function k models the blurring operation, and is called the *point spread function* (PSF). In many applications the kernel satisfies $k(x,y;\xi,\eta) = k(x-\xi, y-\eta)$, and the blur is said to be spatially invariant.

By the Fourier optics model for the atmospheric turbulence [5], the PSF k is expressed as

$$k(x,y) = |\mathcal{F}^{-1}\{\mathcal{P}(x,y) e^{\tau\phi(x,y)}\}|^2 \tag{1.2}$$

where $\mathcal{F}^{-1}$ is the inverse the Fourier transform, $\mathcal{P}$ is the mirror pupil function (a characteristic function, that is $\mathcal{P}(x,y)$ is 1 inside the pupil and 0 outside), $\tau = \sqrt{-1}$, and ϕ is the phase distribution of the wavefront. If ϕ is known, then deconvolution (or image deblurring) methods can be used to reconstruct f from equation (1.1). In this paper the key problem is to reconstruct ϕ.

In order to obtain an approximation of ϕ, gradient measurements from a wavefront sensor (WFS) on the telescope are used. We consider reconstructing the wavefront phase by the model

$$\begin{bmatrix} \boldsymbol{\phi}_x \\ \boldsymbol{\phi}_y \end{bmatrix} = \begin{bmatrix} \boldsymbol{D}_x \\ \boldsymbol{D}_y \end{bmatrix} \boldsymbol{\phi} + \boldsymbol{e}_\phi \tag{1.3}$$

where $\boldsymbol{\phi}_x$ and $\boldsymbol{\phi}_y$ are the discrete, noisy measurements of the horizontal and vertical derivatives of $\boldsymbol{\phi}$, $\boldsymbol{D}_x$ and $\boldsymbol{D}_y$ are discrete, horizontal and vertical derivative operators. The precise structure of $\boldsymbol{D}_x$ and $\boldsymbol{D}_y$ depend on geometry of the wavefront sensor

*Department of Mathematics and Computer Science, Emory University. Email: qchu@mathcs.emory.edu.

[6, 7, 8]. More details on constructing $\boldsymbol{D}_x$ and $\boldsymbol{D}_y$ and solving equation (1.3) will be discussed in later sections of this paper.

Once ϕ is reconstructed, and hence the convolution kernel k is known, we can then use deconvolution methods, such as those described in [13, 14], to compute an approximation of the object f. This paper is organized as the following: Section 2 discusses the mathematical model and the approach to solve the wavefront (or, more precisely, the wavefront phase) reconstruction problem; some numerical experiments are supplied in Section 3; finally conclusion is in Section 4.

2. Mathematical Formulation of Wavefront Reconstruction. As mentioned, in practice the wavefront phase cannot be directly obtained; instead, a sensor inside the telescope measures gradients of ϕ, but only on a relatively coarse grid. The measurements on coarse grids will result in one of the difficulties for image restoration because direct reconstruction of the wavefront phase by interpolation from the coarse gradients cannot achieve the required accuracy. This is especially true in cases of poor seeing conditions, when the atmosphere is highly turbulent. Consequently, when using this reconstruction to restore the images of spatial objects, the restored images will probably not be sufficiently clear. To obtain gradient information on a finer grid, we exploit a *Frozen Flow Hypothesis* (FFH).

2.1. Frozen Flow Hypothesis. The FFH assumes that the entire spatial pattern of a random turbulent field is transported along with the wind velocity. Turbulent eddies do not change significantly as they are carried across the telescope by the wind. By the FFH, multiple frames of wavefront phase, or their gradients, can be included for construction of the turbulence on a finer grid. That is, for a short time interval, the wavefront phase and also the gradients are frozen, and by collecting multiple frames of gradient measurements that overlap on adjacent frames, we can obtain additional information for the wavefront reconstruction problem.

Moreover, by the FFH, atmospheric turbulence can be modeled by a series of independent static layers, each moving across the telescope aperture with the prevailing wind at the altitude of the layer. Because of its simplicity, the FFH is frequently used as the basis for numerical studies of telescope imaging performance, particularly in the modeling of *adaptive optics* (AO) systems [12]. While the FFH is observed not to hold in the real world over long time scales, a number of studies have shown that it is a reasonable approximation for short but still interesting periods [1, 2, 3].

To use the FFH to reconstruct wavefront gradients, several frames of data are collected over a short time period, each giving gradient measurements at a different set of grid points. This is illustrated in Figure 2.1. For ease of presentation, we consider only one layer; clearly multiple, overlapping layers will provide even more grid points in regions where the various layers overlap each other. Note that the composite grid resolution depends on the velocity profile.

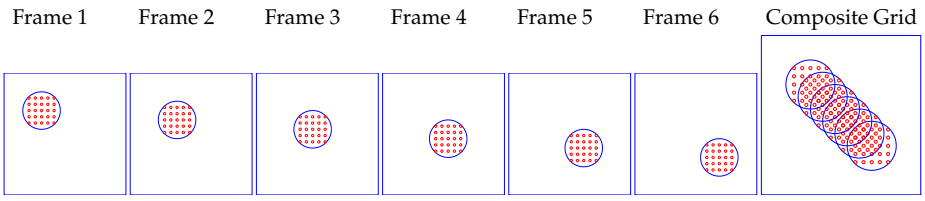

FIG. 2.1. *Illustration of building a composite, high resolution grid using gradient grid points from several frames.*

2.2. Linear Model of the Wavefront Motion. Through appropriate coordinates, we could represent the movement of the wavefront phase and the gradients by shifting their images. Let $\phi(x,y)$ be a function describing the values of the wavefront phase at given positions (x,y), and $\boldsymbol{\phi}$ be a discrete sample of $\phi(x,y)$. That is,

$$\boldsymbol{\phi}(i,j) = \phi(x_i, y_j), \quad i,j = 1,2,\ldots,n.$$

By the FFH, the randomly distributed wavefront phase is moved rigidly. Thus, we could obtain frames of the wavefront phase by shifting the coordinates. The shifting process can be described by a 3×3 affine transformation matrix constructed by the velocity of the wavefront. Let $\boldsymbol{\phi}^{(m)}$ be the mth discretization of $\phi(x,y)$ (the mth frame) of a rigid movement, then

$$\boldsymbol{\phi}^{(m)}(i,j) = \phi(\hat{x}_i, \hat{y}_j), \qquad \text{where} \qquad \begin{bmatrix} \hat{x}_i \\ \hat{y}_j \\ 1 \end{bmatrix} = \begin{bmatrix} a_{11} & a_{12} & a_{13} \\ a_{21} & a_{22} & a_{23} \\ 0 & 0 & 1 \end{bmatrix} \begin{bmatrix} x_i \\ y_j \\ 1 \end{bmatrix}.$$

Note that after shifting, the new coordinates $(\hat{x}_i, \hat{y}_j)$ may not exactly fall onto the original grids, as illustrated in Figure 2.2. That is we may not be able to access the discrete values of the wavefront phase in $\boldsymbol{\phi}$ because only the values on certain grid points are known. To obtain approximate values, we use bilinear interpolation of the

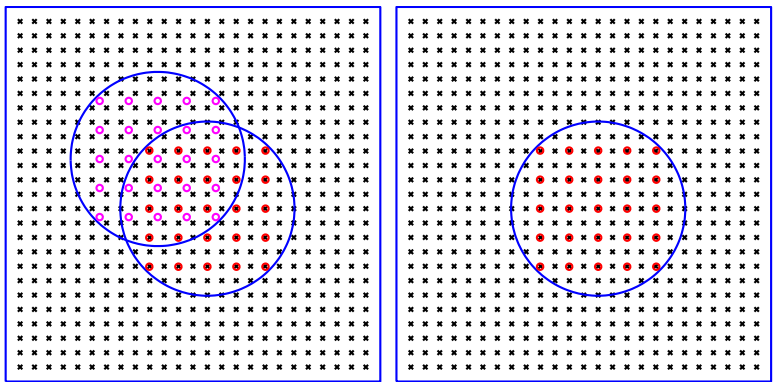

FIG. 2.2. *A single frame of data can be aligned to an underlying, uniform fine grid, as illustrated with the image on the left. However, additional frames are likely to move to locations that do not fall directly on the uniform grid; this is illustrated with the image on the right. In this figure, the x's denote points on the underlying uniform grid, and the o's denote points on the coarse grid of each frame of WFS data.*

most adjacent points surrounding the value of the wavefront phase, or its gradient, on the shifted position $\phi(\hat{x}_i, \hat{y}_j)$. If we assume that the distance between pixel centers is one, then the weights for bilinear interpolation are given as

$$\begin{aligned} \boldsymbol{\phi}^{(m)}(i,j) &= \phi(\hat{x}_i, \hat{y}_j) \\ &\approx (1-\Delta x_i)(1-\Delta y_j)\phi(x_{\hat{i}}, y_{\hat{j}}) + (1-\Delta x_i)\Delta y_j \phi(x_{\hat{i}}, y_{\hat{j}+1}) \\ &\quad + \Delta x_i (1-\Delta y_j)\phi(x_{\hat{i}+1}, y_{\hat{j}}) + \Delta x_i \Delta y_j \phi(x_{\hat{i}+1}, y_{\hat{j}+1}) \end{aligned}$$

where $\Delta x_i = \hat{x}_i - x_i$ and $\Delta y_j = \hat{y}_j - y_j$. In order to define a matrix-vector multiplication to represent the interpolation above, we need to vectorize $\phi = \mathrm{vec}(\phi)$, and so

$\phi^{(m)} = \text{vec}(\phi^{(m)})$. Then we can write

$$\phi^{(m)} = \boldsymbol{A}_m \phi$$

where the matrix A_m is a sparse matrix that contains the interpolation weights. Specifically, the kth row of A_m contains the weights for the pixel in the kth entry of $\phi^{(m)}$. If we use bilinear interpolation, then there are at most four nonzero entries in each row,

$$(1-\Delta x_i)(1-\Delta y_j), \quad (1-\Delta x_i)\Delta y_j, \quad \Delta x_i(1-\Delta y_j), \quad \Delta x_i \Delta y_j.$$

Note that each interpolation matrix A_m contains the velocity information (including both the speed and the direction) which defines Δx_i and Δy_j of each frame.

As mentioned above, we do not know the wavefront phase directly, but a measurement of the gradients. Then a linear formulation of the whole process can be written as

$$\phi_x^{(m)} = \boldsymbol{RWA}_m \boldsymbol{D}_x \phi \quad \text{and} \quad \phi_y^{(m)} = \boldsymbol{RWA}_m \boldsymbol{D}_y \phi$$

where $\boldsymbol{W}$ is an sparse indicator matrix that grabs a certain section of ϕ, and $\boldsymbol{R}$ is a sparse downsampling matrix that transforms high resolution data to a lower resolution. Suppose the number of frames is m, then we have

$$\begin{bmatrix} \phi_x^{(1:m)} \\ \phi_y^{(1:m)} \end{bmatrix} = \begin{bmatrix} (\boldsymbol{I} \otimes \boldsymbol{RW})\boldsymbol{A}\boldsymbol{D}_x \\ (\boldsymbol{I} \otimes \boldsymbol{RW})\boldsymbol{A}\boldsymbol{D}_y \end{bmatrix} \phi$$

where $\boldsymbol{R}$, $\boldsymbol{W}$, $\boldsymbol{D}_x$, $\boldsymbol{D}_y$ were previously defined, $\otimes$ denotes Kronecker product, $\boldsymbol{I}$ is an $m \times m$ identity matrix, and

$$\phi_x^{(1:m)} = \begin{bmatrix} \phi_x^{(1)} \\ \phi_x^{(2)} \\ \vdots \\ \phi_x^{(m)} \end{bmatrix}, \quad \phi_y^{(1:m)} = \begin{bmatrix} \phi_y^{(1)} \\ \phi_y^{(2)} \\ \vdots \\ \phi_y^{(m)} \end{bmatrix}, \quad \boldsymbol{A} = \begin{bmatrix} \boldsymbol{A}_1 \\ \boldsymbol{A}_2 \\ \vdots \\ \boldsymbol{A}_m \end{bmatrix}.$$

In this model, ϕ represents a large, global wavefront phase; but at the time each frame of data is collected, the telescope detects only a small subregion of information, which is modeled by the matrix $\boldsymbol{W}$.

Note that it is impossible to reconstruct the whole global wavefront phase ϕ because we cannot collect enough gradient data to cover the whole wavefront phase region. However, we can construct a composite of the collected information on a high resolution grid by two steps: first, solve two underdetermined least squares problems for the composite x-gradients and y-gradients

$$\phi_z^{\text{composite}} = \arg\min_{\phi_z} \left\| \phi_z^{(1:m)} - (\boldsymbol{I} \otimes \boldsymbol{RW})\boldsymbol{A}\phi_z \right\|_2^2 \tag{2.1}$$

where $z = x, y$; next, use the computed gradients $\hat{\phi}_x^{(i)}$ and $\hat{\phi}_y^{(i)}$, $i = 1, \cdots, m$, from the last step to solve the underdetermined least squares problems for ϕ of each frame

$$\phi^{(i)} = \arg\min_{\phi} \left\| \begin{bmatrix} \hat{\phi}_x^{(i)} \\ \hat{\phi}_y^{(i)} \end{bmatrix} - \begin{bmatrix} \boldsymbol{D}_x \\ \boldsymbol{D}_y \end{bmatrix} \phi \right\|_2^2. \tag{2.2}$$

We remark that both (2.1) and (2.2) are underdetermined, and can be sensitive to noise in the measured data. It is often the case that Tikhonov regularization [14, 15] is incorporated into the least squares formulation, but it is also possible to use truncated iteration methods as well.

2.3. Multi-Layered Atmospheric Model. The previous section focused on the single layer wavefront phase problem. Specifically, the atmosphere above the telescope can be split into several dominant layers, which move with different velocities, and this is a more precise model in practice. For the multi-layered problem, we assume that the composite high resolution wavefront phase at the telescope is the sum of the high resolution wavefront phase at each altitude. Then we have

$$\phi = \sum_{n=1}^{L} c_j \phi_j \tag{2.3}$$

where L is the number of turbulent layers, ϕ is the wavefront phase at the telescope, ϕ_j is the wavefront phase of the jth layer, and c_j is a constant such that $\sum_{j=1}^{L} c_j = 1$ and are used to specify relative dominance in the contribution of each layer to the total turbulent field. For example, if it is assumed that all layers contribute equally to the total wavefront phase hitting the telescope, then $c_1 = c_2 = \cdots = c_L$. On the other hand, if it is assumed that the kth layer is the dominant layer of the atmospheric turbulence, then $c_k \gg c_j$, $j = 1, \cdots, k-1, k+1, \cdots, L$.

Similar to the single layer turbulent model, in the multi-layered case, we model this problem by two steps

$$\begin{bmatrix} \phi_{z,1}^{\text{composite}} \\ \vdots \\ \phi_{z,L}^{\text{composite}} \end{bmatrix} = \arg \min_{\phi_{z,1},\cdots,\phi_{z,L}} \left\| \phi_z^{(1:m)} - (\boldsymbol{I} \otimes \boldsymbol{RW}) \boldsymbol{A}_1 \boldsymbol{D}_x \quad \cdots \quad (\boldsymbol{I} \otimes \boldsymbol{RW}) \boldsymbol{A}_L \begin{bmatrix} c_1 \phi_{z,1} \\ \vdots \\ c_L \phi_{z,L} \end{bmatrix} \right\|_2^2, \tag{2.4}$$

$$\phi^{(i)} = \arg \min_{\phi} \left\| \begin{bmatrix} \hat{\phi}_x^{(i)} \\ \hat{\phi}_y^{(i)} \end{bmatrix} - \begin{bmatrix} \boldsymbol{D}_x \\ \boldsymbol{D}_y \end{bmatrix} \phi \right\|_2^2 \tag{2.5}$$

where $z = x, y$, $\phi_{z,j}^{\text{composite}}$ represents the composite gradients of the jth layer, $j = 1 : L$, $\phi_x^{(1:m)}$, $\phi_y^{(1:m)}$, $\hat{\phi}_x^{(1:m)}$, $\hat{\phi}_y^{(1:m)}$, $\boldsymbol{I}$, $\boldsymbol{R}$, $\boldsymbol{W}$, $\boldsymbol{D}_x$ and $\boldsymbol{D}_y$ are defined as before; $\boldsymbol{A}_j$ denotes the matrix that defines the motion of the atmosphere for layer j. In particular,

$$\boldsymbol{A}_j = \begin{bmatrix} \boldsymbol{A}_{1,j} \\ \boldsymbol{A}_{2,j} \\ \vdots \\ \boldsymbol{A}_{m,j} \end{bmatrix}, \qquad j = 1, 2, \cdots, L$$

where $A_{i,j}$ is the motion matrix for the ith frame of the jth layer. Here we assume there are L layers and m frames for each layer. Again, (2.4) and (2.5) are underdetermined.

3. Numerical Results. For the numerical experiments in this paper, we set some parameters according to practical situations as following: the diameter of the telescope is 3.7 m, the wavelength is 0.744×10^{-6} m, and the propagation distance is 25

km. We only illustrate the efficiency of the multi-layered FFH approach because the single layer approach is a special (and simple) case of it. We assume there are three different turbulent layers in total, and for each layer we assume 50 frames data. The associated data is listed in Table 3.1.

TABLE 3.1
Turbulent layers

layer	location (km)	wind velocity (pixel/frame)	wind direction
1	0	0.1730	horizontally
2	11	0.9686	vertically
3	15	0.5189	diagonally

The size of the least squares system depends on the image size, wind velocity, which decides the size of the composite image, and the downsample size. The image size of each frame is 256 by 256. Using the above wind velocity, the composite size is 304 by 304. The size of the downsampling image is 64 by 64. Therefore, the size of the least squares problem in (2.4) is 204800 by 277248.

Another important parameter to measure the severity of the blurring is the ratio between the telescope diameter D and the Fried parameter r_0. In physics, the smaller the ratio $\frac{D}{r_0}$ is, the less turbulence is involved in the captured images. In general if $\frac{D}{r_0}$ is less than 20, then the captured images are not too blurred as shown in Figure 3.3; otherwise, the wavefront is highly oscillatory, and so the captured images are much more blurred, as shown in Figure 3.9.

We apply Tikhonov regularization to solve (2.4) by setting regularization parameter $1000\sqrt{\epsilon}$, where ϵ is the machine precision, and LSQR as the solver.

3.1. Experiment 1. First, we consider the case when $\frac{D}{r_0} = 5$, and thus the wavefront is very smooth, and there is very little blur in observed image. Three different approaches are used: the multi-layered FFH approach, the single layer FFH approach and a naive approach which is simply to resize the gradients information. The reconstructed composite gradients and phase is shown in Figure 3.1. Figure 3.2 shows the comparison of the relative errors of the reconstructed PSF, and Figure 3.3 is the true image and the reconstructed image by the three approaches.

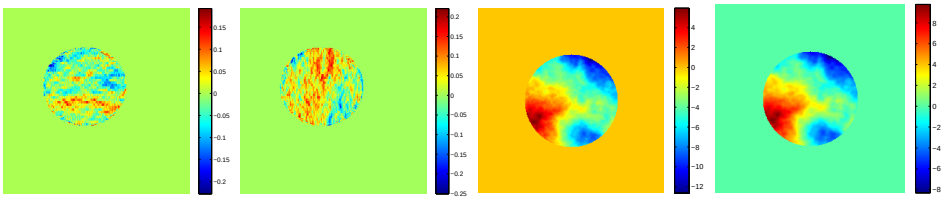

FIG. 3.1. *From left to right (by multi-layered FFH approach, $\frac{D}{r_0} = 5$): the 1st layer of composite x-gradients, the 1st layer of composite y-gradients, the 1st frame of the true phase, and the 1st frame of the reconstructed phase. The regions of the composite gradients are consistent with the turbulent direction (horizontally) of the first layer.*

3.2. Experiment 2. Next, we consider $\frac{D}{r_0} = 20$, which means that the wavefront has nontrivial oscillations, and the observed image contains a significant amount of blurring. Again, the above three different approaches are used. The reconstructed

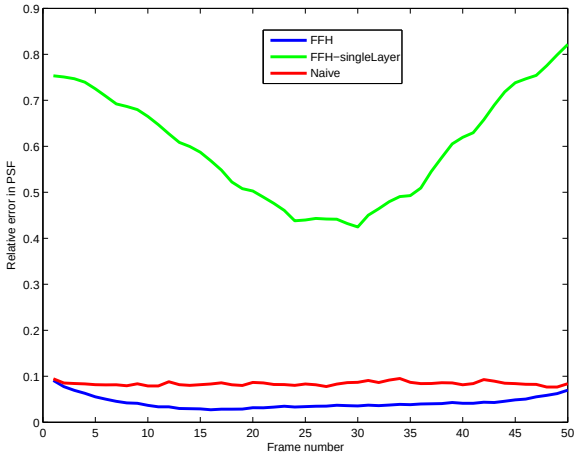

FIG. 3.2. *Compare the relative error of the reconstructed PSF from the three different approaches when* $\frac{D}{r_0} = 5$.

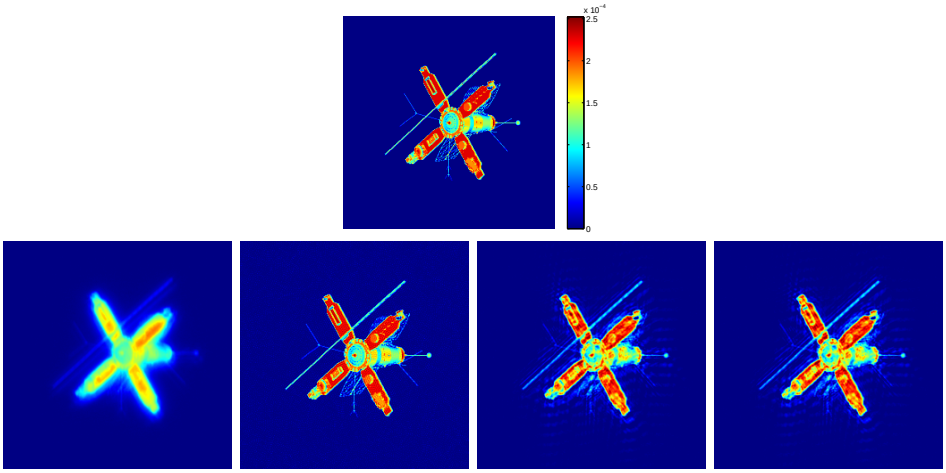

FIG. 3.3. *Top: the true object. From left to right (*$\frac{D}{r_0} = 5$*) : the 1st frame of the observed blurred image (the blur is not too significant), the reconstructed image by multi-layered FFH model, the reconstructed image by single layer FFH model, the reconstructed image by naive approach.*

composite gradients and phase is shown in Figure 3.4. Figure 3.5 shows the comparison of the relative errors of the reconstructed PSF, and Figure 3.6 is the true image and the reconstructed image by the three approaches.

3.3. Experiment 3. Finally, we consider $\frac{D}{r_0} = 45$. In this case, the wavefront is highly oscillatory and the observed images are severely blurred. Three different approaches are used. The reconstructed composite gradients and phase is shown in Figure 3.7. Figure 3.8 shows the comparison of the relative errors in PSF, and Figure 3.9 is the true image and the reconstructed image by the three approaches.

4. Conclusions. Note that the least squares problem (2.4) only depends on the wind velocity. Thus the structure of the coefficient matrix, such as the number of non-zero entries does not change with $\frac{D}{r_0}$. In fact, the number of non-zeros in (2.4)

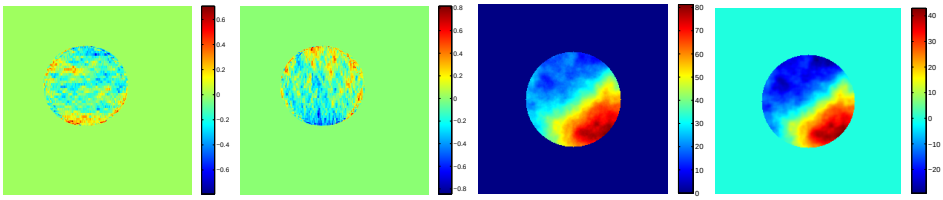

FIG. 3.4. *From left to right (by multi-layered FFH approach, $\frac{D}{r_0} = 20$): the 1st layer of composite x-gradients, the 1st layer of composite y-gradients, the 1st frame of the true phase, and the 1st frame of the reconstructed phase. The regions of the composite gradients are consistent with the turbulent direction (horizontally) of the first layer.*

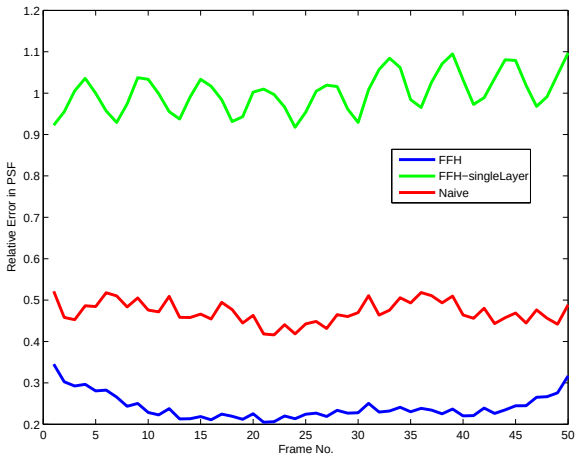

FIG. 3.5. *Compare the relative error of the reconstructed PSF from the three different approaches when $\frac{D}{r_0} = 20$.*

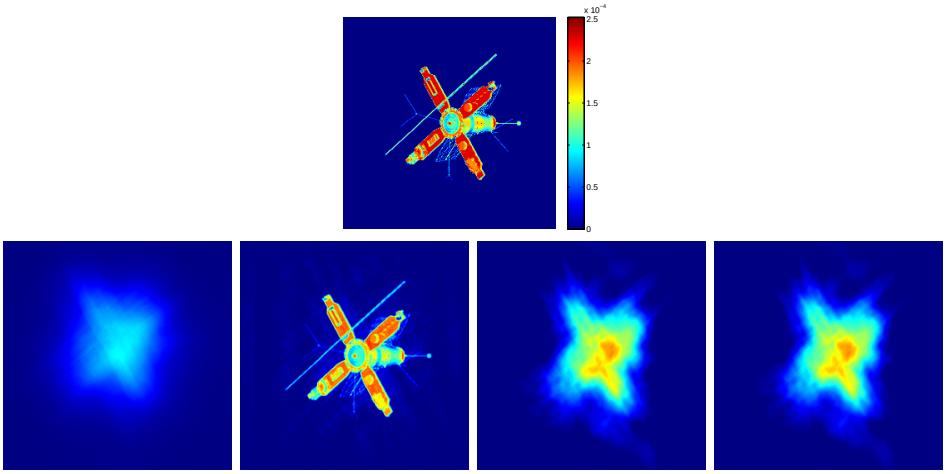

FIG. 3.6. *Top: the true object. From left to right ($\frac{D}{r_0} = 20$) : the 1st frame of the observed blurred image (the blur is quite significant), the reconstructed image by multi-layered FFH model, the reconstructed image by single layer FFH model, the reconstructed image by naive approach.*

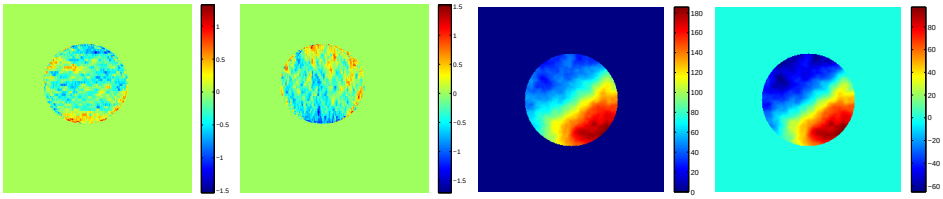

FIG. 3.7. *From left to right (by multi-layered FFH approach, $\frac{D}{r_0} = 45$): the 1st layer of composite x-gradients, the 1st layer of composite y-gradients, the 1st frame of the true phase, and the 1st frame of the reconstructed phase. The regions of the composite gradients are consistent with the turbulent direction (horizontally) of the first layer.*

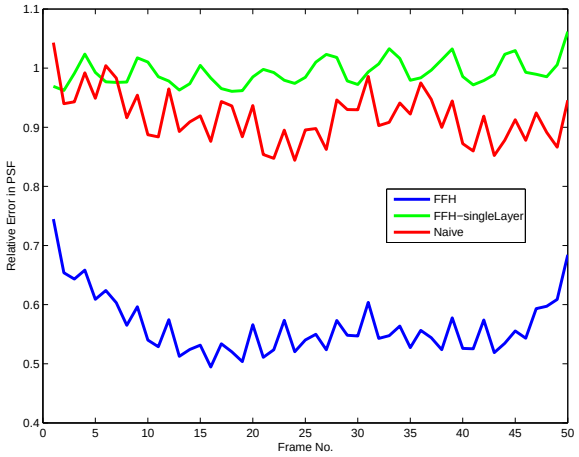

FIG. 3.8. *Compare the relative error of the reconstructed PSF from the three different approaches when $\frac{D}{r_0} = 45$.*

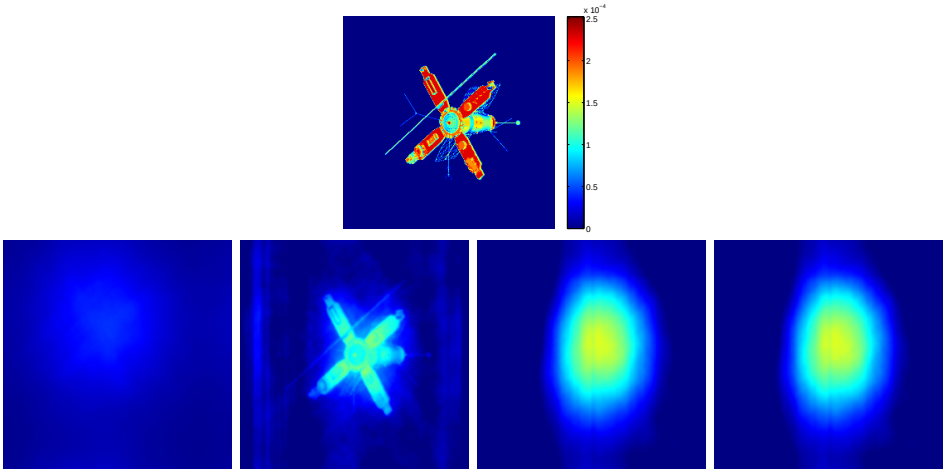

FIG. 3.9. *Top: the true object. From left to right ($\frac{D}{r_0} = 45$) : the 1st frame of the observed blurred image (the blur is very significant), the reconstructed image by multi-layered FFH model, the reconstructed image by single layer FFH model, the reconstructed image by naive approach.*

is 2616204. Since the size and the number of non-zeros do not change over $\frac{D}{r_0}$, the number of iterations does not change:

TABLE 4.1
Iterative Information

ϕ_z ($\frac{D}{r_0}$)	number of iterations	relative residual
ϕ_x (5)	20	0.0266
ϕ_y (5)	20	0.0255
ϕ_x (20)	20	0.0211
ϕ_y (20)	20	0.0241
ϕ_x (45)	20	0.0200
ϕ_y (45)	20	0.0228

Based on the experiments, the multi-layered FFH is robust in different cases of $\frac{D}{r_0}$. Especially when $\frac{D}{r_0}$ is relatively large, the relative error in PSF and the reconstruction of object using our multi-layered FFH approach is much better than the the standard naive interpolation approach, as well as the single layer model.

We observe that the relative error of the reconstructed PSF depends on the frame number (note the oscillations in the relative error plots). This behavior can be explained as follows. Because of the movement of the turbulent eddies, the overlap regions may vary, and thus the corresponding contributions vary.

REFERENCES

[1] E. Gendron and P. Léna, Single Layer Atmospheric Turbulence Demonstrated by Adaptive Optics Observations, Astrophysics and Space Science, 239(1996), pp. 221-228.
[2] L. A. Poyneer and M. van Dam and J. P. Véran, Experimental Verification of the Frozen Flow atmospheric Turbulence Assumption with Use of Astronomical Adaptive Optics Telemtry, J. Opt. Soc. Am. A, 26(2009), pp.833-846.
[3] M. Schöck and E. J. Spillar, Method for a Quantitative Investigation of the Frozen Flow Hypothesis, J. Opt. Soc. Am. A, 17(2000), pp.1650-1658.
[4] E. Gershnik, E.N. Ribak, Light Propagation through Multilayer Atmosperic Turbulence, Optics Communications, Oct. 1997.
[5] Michael C. Roggemann, Byron M. Welsh, Imaging through Turbulence, CRC-Press, March 18, 1996.
[6] D. L. Fried, Least-Square Fitting a Wave-front Distortion Estimate to an Array of Phase-Difference Measurements, J. Opt. Soc. Am, 67(3):370-375, 1977.
[7] R. H. Hudgin, Wave-front Reconstruction for Compensated Imaging, J. Opt. Soc. Am, 67(3):375-378, 1977.
[8] J M. Bardsley and S Knepper and J G Nagy, Structured Linear Algebra Problems in Adaptve Optics Imaging, Comp. Math, 2011.
[9] Jason D. Schmidt, Numerical Simulation of Optical Wave Propagation with Examples in MATLAB, SPIE Press, August 5, 2010.
[10] Johnathan M. Bardsley, Wavefront Reconstruction Methods for Adaptive Optics Systems on Ground-Based Telescopes, SIAM Journal on Matrix Analysis and Application, Volume 30 Issue 1, 2008, pp. 67-83.
[11] Johnathan M. Bardsley, An Analysis of Methods for Wavefront Reconstruction From Gradient Measurements in Adaptive Optics, Int. J. of Pure and Applied Mathematics, Vol. 42, No. 1, 2008, pp. 71-81.
[12] Jacques M. Beckers, Adaptive Optics for Astronomy: Principles, Performance, and Applications, Annu. Rev. Astron. Astrophs., 1993, 31, pp. 13-62.
[13] C. R. Vogel, Computational Methods for Inverse Problems, SIAM, Philadelphia, 2002.
[14] A. N. Tikhonov, A. V. Goncharsky, V. V. Stepanov and A. G. Yagola, Numerical Methods for the Solution of Ill-Posed Problems, Kluwer Academic Publishers, 1990.
[15] C. W. Groetsch, The Theory of Tikhonov Regularization for Fredholm Integral Equations of the First Kind, Pitman, Boston, 1984.